POLITECNICO DI TORINO
Repository ISTITUZIONALE

LUT-less Sensorless Control of Synchronous Reluctance Machines using the Locus of Incremental Saliency Ratio Tracking (LIST)

(Article begins on next page)

18 October 2022

LUT-less Sensorless Control of Synchronous Reluctance Machines using the Locus of Incremental Saliency Ratio Tracking (LIST)

Anantaram Varatharajan, *Member*, Gianmario Pellegrino, *Senior Member*, Guilherme Bueno Mariani, *Member*, Nicolas Voyer and Akira Satake

Abstract—This paper deals with the LUT-less sensorless control of synchronous reluctance (SyR) machines at zero and low speeds, where LUT-less stands for avoiding the use of flux-map look-up tables (LUTs) or other pre-determined machine parameters. The new signal-injection based control scheme called the Locus of Incremental Saliency ratio Tracking (LIST) is presented, where a pulsating high-frequency voltage component is used for position tracking and a second rotating signal-injection is dedicated to on-line estimating the incremental saliency ratio. A trajectory of constant incremental saliency ratio is used for torque regulation, resulting in stable control at all operating conditions, including overload. This despite the effect of cross-saturation, which is known to introduce position error and harm the control stability progressively with the load. The proposed scheme is validated experimentally on a 1.1 kW SyR machine test-bench. Alternative LUT-less torque control laws are investigated, and their stability limits put in evidence using convergence analysis and experiments.

Index Terms—Sensorless control, signal-injection, incremental saliency ratio, synchronous reluctance machine.

I. INTRODUCTION

Sustained load operation at low speeds is an attractive feature that is increasingly required in general purpose sensorless motor drives. Typically, position estimation in the zero-speed region is obtained by tracking the incremental saliency via high-frequency response. In literature, such methods can be divided into two categories: continuous excitation using periodic signal-injection [1]–[3] and discontinuous excitation schemes [4]–[6].

Irrespective of the type of excitation, the efficacy of most sensorless techniques relies on the accuracy of the flux-map look-up tables (LUTs) of the machine under test, especially for synchronous reluctance (SyR) motors [6], dictating a dedicated

preliminary session of machine identification. To date, the most advanced forms of plug-and-play control of SyR motor drives rely on sensorless LUTs self-commissioning methods such as the ones in [7]–[9]. A flux-map LUT-less position observer is highly desired for the wider and flexible application of SyR motors in general purpose variable speed drives.

Among the various forms of high-frequency signal-injection, the pulsating voltage injection along the estimated $\hat{d}$-axis, and particularly the square-wave injection, is retained favorable for the superior dynamic response [1], [2]. When using the high-frequency current response in the estimated $\hat{q}$-axis for position tracking, the cross-saturation position error exists that is very prominent in SyR machines and harms the control stability under load [10], [11]. All cross-saturation error compensation techniques such as current compensation [12]–[14], angle compensation [15]–[17] and tilted-axis voltage injection [18]–[20] are flux-map LUTs dependent. The convergence analysis of [18]–[20] is a powerful stability assessment tool that shows how the lack of cross-saturation error compensation harms the stability of control very prematurely, besides impairing the accuracy of position estimation. Another LUTs-dependent aspect of the control of SyR machines is the selection of the appropriate dq reference values for current vector control (CVC) according to the torque request and the respect of the maximum-torque-per-ampere (MTPA) law. This is normally retrieved via additional current reference LUTs, obtained processing the flux-map LUTs, which is incompatible with a LUT-less control scheme. However, simplified torque control laws such as constant d-axis current or constant current phase angle γ result nonviable in sensorless control, as demonstrated in the paper, posing an additional challenge.

This paper presents a stable sensorless control technique for SyR machines without preliminary identification of the motor under control, foreseeing the possibility of brand-independent, plug-and-play control for general purpose applications. The new method referred to as the Locus of Incremental Saliency ratio Tracking (LIST) is proposed, where the incremental saliency ratio (isr) is on-line estimated and one suitable value of constant isr is used as the torque control law. As opposed to using a predefined current reference trajectory (such as MTPA), the LIST technique uses adaptive current reference and overcomes the stability problems of the position observer due to the cross-saturation error at all torque values, including overload conditions, without requiring compensation of the
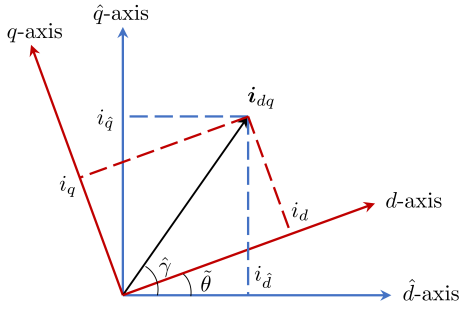
Fig. 1. Illustration of the estimated $\hat{d}q$ synchronous rotor reference frame whose $\hat{d}$-axis is at $\tilde{\theta} = \theta - \hat{\theta}$ from the real d-axis.
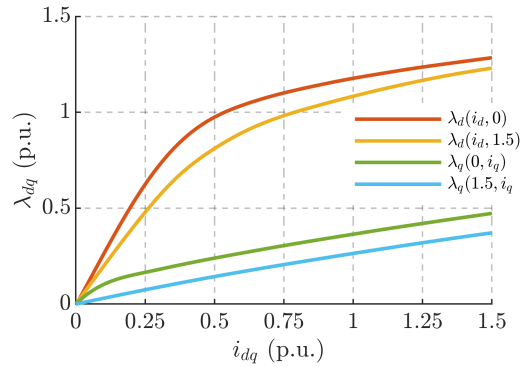

Fig. 2. Flux map of the SyR motor under test exhibiting saturation and cross-saturation characteristics. Experimentally identified with the constant speed test, reported in [21].

position error.

The main contributions of the paper are enumerated as follows:

1) The LIST is realized using the real-time estimation of isr and tracking of a constant isr locus with the $\hat{d}$-axis current regulation.

2) The real-time computation of isr uses an elliptical voltage injection, for on-line incremental inductance estimation.

3) A standard signal-injection based position observer is used, prone to cross-saturation position error.

4) The novelty of the LIST concept lies in the immunity of the constant isr trajectory in the estimated reference from the cross-saturation induced stability problems. The cross-saturation position error is therefore acceptable and this makes LUT-less control feasible.

5) Alternative torque control laws usable in non-sensorless control such as constant current angle locus and constant $\hat{d}$-axis current locus are investigated using the convergence analysis, showing their noncompliance.

The paper is organized as follows: the mathematical framework of sensorless control system and the notion of incremental saliency ratio is introduced in Section II. The signal-injection position estimation based on square-wave pulsating injection is briefed in Section III. The stability problems arising from the cross-saturation effects are discussed using convergence analysis in Section IV. The proposed LIST control scheme is discussed in Section V. The experimental validation on a 1.1 kW SyR motor is presented in Section VI and finally, Section VII concludes the paper.

II. SENSORLESS CONTROL SYSTEM

The electrical rotor position is θ and the electrical angular speed is $\omega = s\,\theta$ where s is the differential operator $\frac{d}{dt}$. Estimated vectors are represented by the superscript ˆ. The orthogonal rotational matrix is $\mathbf{J} = \begin{bmatrix} 0 & -1 \\ 1 & 0 \end{bmatrix}$ and $\mathbf{I}$ is the identity matrix. Real space vectors will be used; for example, the stator current is $\boldsymbol{i}_{dq} = [i_d, i_q]^{\mathrm{T}}$ where i_d and i_q are the vector components in the rotor reference frame.

A. Synchronous Reluctance Machine Model

The machine model is expressed in coordinates of estimated rotor reference frame, denoted by subscript $\hat{d}q$, whose $\hat{d}$-axis

is at $\hat{\theta} = \theta - \tilde{\theta}$, as shown in Fig. 1 where $\tilde{\theta}$ is the position error. The voltage equation of a synchronous machine is

$$s\,\boldsymbol{\lambda}_{\hat{d}q} = \boldsymbol{v}_{\hat{d}q} - R_s\boldsymbol{i}_{\hat{d}q} - \hat{\omega}\,\mathbf{J}\,\boldsymbol{\lambda}_{\hat{d}q} \tag{1}$$

where R_s is the stator resistance and $\boldsymbol{\lambda}_{\hat{d}q}$ is the stator flux linkage. The electromagnetic torque is given by

$$T = \frac{3p}{2}\,\boldsymbol{i}_{\hat{d}q}^{\mathrm{T}}\,\mathbf{J}\,\boldsymbol{\lambda}_{\hat{d}q} \tag{2}$$

where p is the number of pole pairs.

Let $\boldsymbol{\Lambda}_{dq}(\boldsymbol{i}_{dq})$ denote the 2-D flux-map LUTs of the machine under test, shown in Fig. 2. Then, the stator flux linkage in the estimated reference frame can be expressed as

$$\boldsymbol{\lambda}_{\hat{d}q} = \mathrm{e}^{\mathbf{J}\tilde{\theta}}\,\boldsymbol{\Lambda}_{dq}(\mathrm{e}^{-\mathbf{J}\tilde{\theta}}\,\boldsymbol{i}_{\hat{d}q}). \tag{3}$$

B. Small-Signal Machine Model

The time derivative of the stator flux linkage in the estimated rotor reference frame can be expressed as

$$s\,\boldsymbol{\lambda}_{\hat{d}q} = \mathrm{e}^{\mathbf{J}\tilde{\theta}}\,\boldsymbol{L}_\partial\,\mathrm{e}^{-\mathbf{J}\tilde{\theta}}\,\boldsymbol{i}_{\hat{d}q} \tag{4}$$

where the incremental inductance matrix $\boldsymbol{L}_\partial$ is a function of the operating point $\boldsymbol{i}_{dq}$, given by

$$\frac{\partial\boldsymbol{\lambda}_{dq}}{\partial\boldsymbol{i}_{dq}} = \boldsymbol{L}_\partial(\boldsymbol{i}_{dq}) = \begin{bmatrix} l_d & l_{dq} \\ l_{dq} & l_q \end{bmatrix} \tag{5}$$

where l_d, l_q represents the incremental inductance along the d and q-axes, respectively, while l_{dq} is the cross-saturation term.

Due to the cross-saturation inductance l_{dq} in (5), the direction of the maximum incremental inductance is not aligned with the d-axis. The magnetic incremental saliency is deviated from the geometric axis by an angle referred to as the cross-saturation position error, given by

$$\tilde{\theta}_{dq} = -\frac{1}{2}\tan^{-1}\frac{l_{dq}}{l_\Delta} \tag{6}$$

where $l_\Delta = (l_d - l_q)/2$. Otherwise said, the angle $\tilde{\theta}_{dq}$ is the phase displacement between the direction of the maximum incremental inductance and the d-axis. The contour of the cross-saturation position error (6) in the dq current plane for the SyR machine under test is shown in Fig. 3(a).
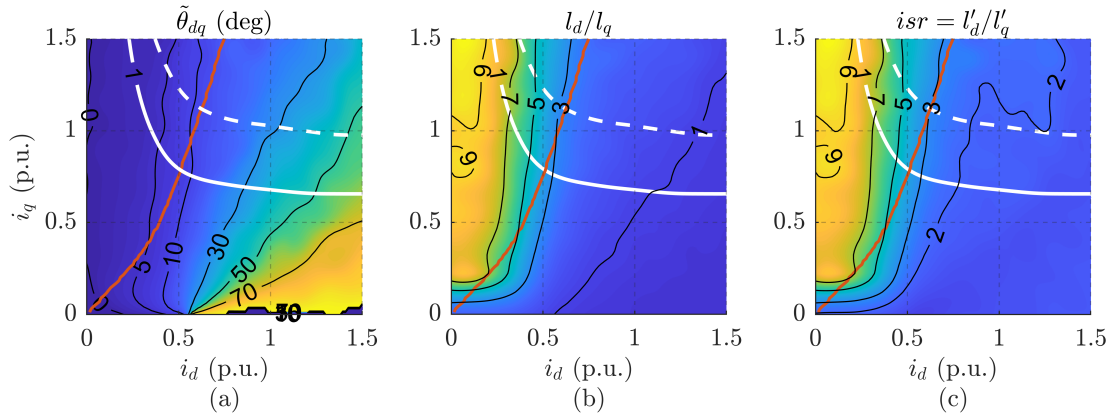
Fig. 3. Contours in the dq current plane: (a) Cross-saturation position error (6); (b) Ratio of d-axis to q-axis incremental inductance; (c) Incremental saliency ratio (9). Red line is the MTPA trajectory. White lines represent the torque contour for the levels 1 p.u. and 1.5 p.u. (dashed).

In turn, the incremental inductance (5) takes the form of a diagonal matrix if rotated by the angle $\tilde{\theta}_{dq}$, i.e., (5) can be reformulated as

$$\boldsymbol{L}'_{\partial} = \mathrm{e}^{\mathbf{J}\tilde{\theta}_{dq}}\, \boldsymbol{L}_{\partial}\, \mathrm{e}^{-\mathbf{J}\tilde{\theta}_{dq}} \qquad \boldsymbol{L}'_{\partial} = \begin{bmatrix} l'_d & 0 \\ 0 & l'_q \end{bmatrix} \qquad (7)$$

where l'_d and l'_q represent the maximum and minimum incremental inductance for a given $\boldsymbol{i}_{dq}$ operating point, respectively. The terms of the diagonal incremental inductance matrix (7) are given by

$$\boldsymbol{L}'_{\partial} = \begin{bmatrix} l_{\Sigma} + \sqrt{l_{\Delta}^2 + l_{dq}^2} & 0 \\ 0 & l_{\Sigma} - \sqrt{l_{\Delta}^2 + l_{dq}^2} \end{bmatrix} \qquad (8)$$

where $l_{\Sigma} = (l_d + l_q)/2$. The incremental saliency ratio (isr) is defined as the ratio of maximum to minimum incremental inductance, as

$$isr = \frac{l'_d}{l'_q} = \frac{l_{\Sigma} + \sqrt{l_{\Delta}^2 + l_{dq}^2}}{l_{\Sigma} - \sqrt{l_{\Delta}^2 + l_{dq}^2}}. \qquad (9)$$

It can be discerned that (9) is always greater than one, i.e., $isr \geq 1$. The contours of ratio l_d/l_q and the isr are shown in Figs. 3(b) & 3(c), respectively; they are observed to be largely similar in the regions of high current angle where the cross-saturation effect is weak. It is also worth pointing out that, at very high i_d, the inverse saliency $l_d/l_q < 1$ occurs.

III. SIGNAL-INJECTION POSITION OBSERVER

Let the subscript $\hat{d}qh$ denote the high-frequency terms in the estimated $\hat{d}q$ reference frame.

A. Pulsating Voltage Injection

Let the superscript k denote the discrete domain representation of the kth sampling instant. In this work, a pulsating voltage injection in the form of square-wave voltage at half the switching frequency is injected along the estimated $\hat{d}$-axis, expressed as

$$\left(v_{\hat{d}h}^*\right)^k = V_{sw} \cos\left(\pi k\right) = \begin{cases} +V_{sw}, & \text{if } k == 2n \\ -V_{sw}, & \text{if } k == 2n+1 \end{cases} \qquad (10)$$

where V_{sw} is the magnitude and n is an integer; the superscript $*$ is used to denote the reference quantities. The square-ware injection is chosen for its ease of implementation and high-dynamic performance [1]. Nevertheless, the following analysis in this paper is also valid for the sinusoidal pulsating injection.

Let Δ symbolize the discrete operation

$$\Delta x^k = x^k - x^{k-1}. \qquad (11)$$

Then, the high-frequency current corresponding to the square-wave voltage injection (10) is given by

$$\boldsymbol{i}_{\hat{d}qh}^k = \Delta\, \boldsymbol{i}_{\hat{d}q}^k. \qquad (12)$$

Typically, the stator resistance and the back-emf voltage terms are insignificant at low speeds in the high-frequency domain and can be neglected, i.e.,

$$\boldsymbol{\lambda}_{\hat{d}qh}^k \approx T_s \begin{bmatrix} v_{\hat{d}h}^{k-1} \\ 0 \end{bmatrix} \qquad (13)$$

where T_s is the sampling interval. Note that, due to the unit digital delay, the voltage actuated at the instant k corresponds to the reference computed at the instant $k-1$, i.e.,

$$\boldsymbol{v}_{dq}^k = \left(\boldsymbol{v}_{dq}^*\right)^{k-1} \quad \Rightarrow \quad \boldsymbol{\lambda}_{\hat{d}qh}^k \approx T_s \begin{bmatrix} \left(v_{\hat{d}h}^*\right)^{k-2} \\ 0 \end{bmatrix}. \qquad (14)$$

B. Position Error Signal

Conventionally, the position error signal ϵ is derived from the high-frequency current response in the direction orthogonal to the axis of injection, i.e., $\hat{q}$-axis current $i_{\hat{q}h}$. It follows from (4) and (7) that

$$\boldsymbol{i}_{\hat{d}qh}^k = \mathrm{e}^{\mathbf{J}(\tilde{\theta}-\tilde{\theta}_{dq})}\, \boldsymbol{L}_{\partial}'^{-1}\, \mathrm{e}^{-\mathbf{J}(\tilde{\theta}-\tilde{\theta}_{dq})}\, \boldsymbol{\lambda}_{\hat{d}qh}^k. \qquad (15)$$

Simplifying (15), the high-frequency $\hat{q}h$-axis current can be expressed as

$$i_{\hat{q}h}^k = -T_s \left(v_{\hat{d}h}^*\right)^{k-2} \cdot \frac{isr-1}{l'_d} \sin\left(2\tilde{\theta} - 2\tilde{\theta}_{dq}\right). \qquad (16)$$

Following (16), the position error signal ϵ to the phase-locked-loop (PLL) (19) can be designed from $i_{\hat{q}h}$ as

$$\epsilon^k = \cos\left(\pi(k-2)\right) \frac{i_{\hat{q}h}^k}{i_0} \qquad (17)$$
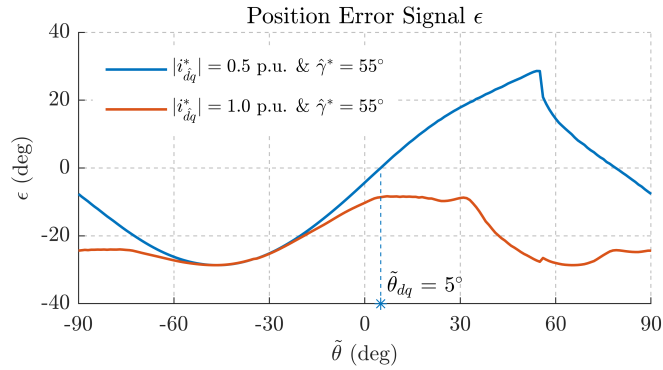
Fig. 4. Position error signal (17) as a function of position error for two different operating points in the estimated $\hat{d}q$ reference frame.
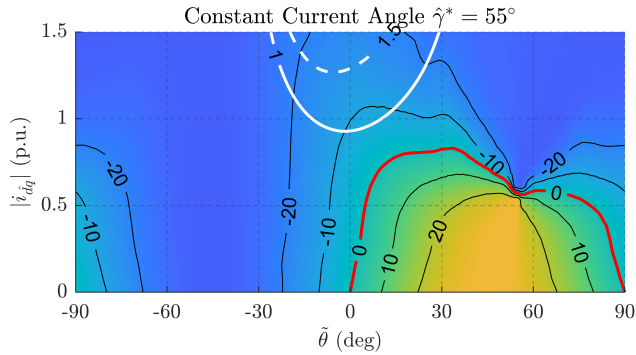

Fig. 5. Position error signal (17) contour for the current references using a constant current angle $\hat{\gamma}^* = 50°$ in the estimated $\hat{d}q$ reference frame. Red line is the zero contour of the error signal. White lines represent the torque contour levels 1 p.u. and 1.5 p.u. (dashed).

where the gain i_0 for appropriate scaling is given by

$$i_0 = -2\,T_s\,V_{sw}\,\frac{isr - 1}{l'_d}. \qquad (18)$$

An accurate gain i_0 (18) is assumed in the following sections which holds true if the incremental inductances (and isr) are estimated on-line. The superscript k is considered implicit and is dropped in the following sections.

C. Speed and Position Observer

A conventional PLL with a proportional-integral (PI) controller is employed to drive the position error signal ϵ to zero as

$$\hat{\omega} = k_p\,\epsilon + \int k_i\,\epsilon\,\mathrm{d}t \qquad \hat{\theta} = \int \hat{\omega}\,\mathrm{d}t \qquad (19)$$

where k_p and k_i are the respective gains. The gains of the PLL are tuned for a critically damped response considering $\epsilon = \tilde{\theta}$ by placing the two poles at $s = -\Omega_\omega$: $k_p = 2\,\Omega_\omega$ & $k_i = \Omega_\omega^2$.

IV. STABILITY ASSESSMENT

The application of classical stability analysis such as transfer function and state-space approaches to the high-frequency excitation-based position observers is challenging. This is due to the difficulty in modeling (linearizing) the incremental inductance and isr which are very nonlinear. The state-of-art
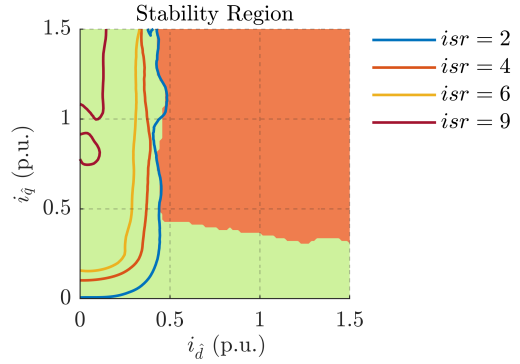

Fig. 6. Feasible region of operation (green) in the estimated $\hat{d}q$ reference frame; the operating points in the red region have no convergence and are unstable.

approach for stability assessment is the convergence analysis developed in [18]–[20].

A. Convergence Analysis

The position error signal (17) is a function of the operating point in the estimated $\hat{d}q$ reference frame and the position error, i.e., $\epsilon(\boldsymbol{i}_{\hat{d}q}, \tilde{\theta})$. The PLL converges to a steady-state condition only if the input position error signal converges to zero and in particular, a stable equilibrium is established if the position error signal has a positive slope around zero. The position error at which the error signal has a zero-crossing with a positive slope (zero-up crossing) is the steady-state position error. It can be shown analytically from (16) and (17) that the steady-state position error for a given current reference $\boldsymbol{i}_{\hat{d}q}^*$, if convergence exists, is equal to the cross-saturation error (6):

$$\epsilon(\boldsymbol{i}_{\hat{d}q}, \tilde{\theta})\Big|_{\boldsymbol{i}_{\hat{d}q}=\boldsymbol{i}_{\hat{d}q}^*} = 0 \quad \Rightarrow \quad \tilde{\theta} = \tilde{\theta}_{dq}. \qquad (20)$$

Given one operating point in the estimated $\hat{d}q$ frame, the convergence analysis determines whether the convergence condition exists (i.e., stable control with stationary position error) or not (unstable control). Using (16)-(18), the position error signal $\epsilon(\boldsymbol{i}_{\hat{d}q}, \tilde{\theta})$ is computed as a function of position error $\tilde{\theta}$ for two selected current reference data points and is shown in Fig. 4. Please notice that the operating points are defined in the estimated reference frame where the currents are assumed to be tracking the reference point, $\boldsymbol{i}_{\hat{d}q} = \boldsymbol{i}_{\hat{d}q}^*$. It is worth pointing out that the inductance in (16) are also a function of the position error, $\boldsymbol{L}'_\partial(\mathrm{e}^{\mathbf{J}\tilde{\theta}}\,\boldsymbol{i}_{\hat{d}q})$. The following inferences are drawn from Fig. 4:

- The reference point $|\boldsymbol{i}_{\hat{d}q}^*| = 0.5$ p.u. & $\hat{\gamma}^* = 55°$ (blue line in Fig. 4) has a zero-up crossing at $\tilde{\theta} = 5°$ which is the steady-state position error. This is mapped to the real dq plane with current angle $\gamma = \hat{\gamma}^* - \tilde{\theta} = 50°$ which coincides with the contour level $\tilde{\theta}_{dq} = 5°$ in Fig. 3(a). In turn, a current angle of $\gamma = 50°$ is obtained when commanding $\hat{\gamma}^* = 55°$.
- The reference point $|\boldsymbol{i}_{\hat{d}q}^*| = 1.0$ p.u. & $\hat{\gamma}^* = 55°$ (red line) has no zero-up crossings, implying that the PLL diverges to instability. In other words, this reference point in the
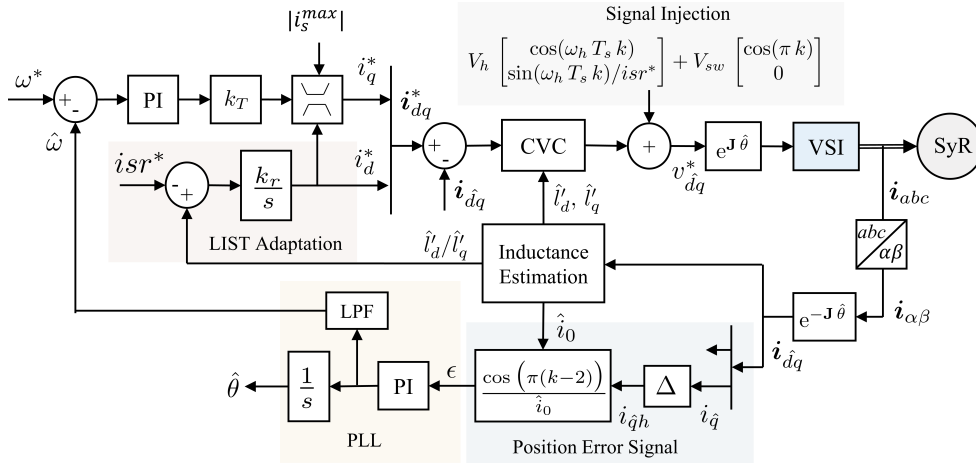
Fig. 7. Block diagram of the proposed position observer using CVC highlighting the LIST adaptation for the $\hat{d}$-axis current reference, signal-injection block comprising of a rotating elliptical voltage and a pulsating square-wave voltage, position error signal estimation and the PLL.

$\hat{d}q$ coordinates is not mapped to the real dq current plane due to the cross-saturation error.

Extending the analysis in Fig. 4 to all data points with a constant reference current angle $\hat{\gamma}^* = 55°$, the contour plot in Fig. 5 is obtained. The nominal and 150% torque contours are also reported, in white. It can be discerned that the rated torque has no stable zero-up crossing and is unattainable. Such contour plots are the standard signature of the convergence analysis to illustrate the stability limits.

B. Feasible Regions of Operation

The feasible operating points in the estimated $\hat{d}q$ reference frame are defined as those that have a stable convergence (zero-up crossing). For a comprehensive assessment of feasibility, the analysis similar to Fig. 4 is performed on each reference data point $i^*_{\hat{d}q}$ in the dq current plane. The following inferences are drawn from Fig. 6:

- The region in red denotes the unfeasible operating points with no convergence. It is observed that a substantial section of the plane is inoperable which is unknown a priori without the flux-map LUTs. This finding is valid in general for all SyR machines.
- The isr trajectories in Fig. 3(c) in the dq reference frame are displaced by the cross-saturation error in Fig. 3(a) when referred to the estimated $\hat{d}q$ reference frame in Fig. 6. All data points in Fig. 3(c) are mapped to the feasible region in green that is visibly shrunk.

Thus, attention must be paid in defining the reference current trajectory, when cross-saturation effects cannot be compensated. As the optimal MTPA current angle for SyR machines is typically between $45° < |\gamma| < 75°$, a constant current angle locus can be envisaged as a viable approximation of the MTPA trajectory. However, the convergence analysis for $\hat{\gamma}^* = 55°$ in Fig. 5 shows that the rated torque is unattainable. Fig. 6 suggests an increased stability for higher current angles as indeed the convergence analysis for $\hat{\gamma}^* = 70°$ (see Fig. 14 in Appendix) shows where the rated torque is attainable but the overload remains unfeasible.

As an alternative to the constant current angle locus, the feasibility of using a constant $\hat{d}$-axis current locus as the $i^*_{\hat{d}q}$ reference trajectory is investigated (see Figs. 15 & 16 in Appendix). Although the choice $i^*_{\hat{d}} = 0.25$ p.u. averts the stability problems corroborating Fig. 6, the suitable choice of $i^*_{\hat{d}}$ is machine-dependent and the generality questionable in the absence of exhaustive analysis using the flux-map information.

V. PROPOSED LIST CONTROL SCHEME

In the absence of flux-map and MTPA LUTs, a method is sought to translate the torque output of the speed controller into $i^*_{\hat{d}q}$ current references. An ideal reference current trajectory should lie in feasible region in Fig. 6 such that every operating point in the estimated $\hat{d}q$ reference frame is mapped to the real dq current plane.

A. Locus of Incremental Saliency Tracking (LIST)

The LIST idea originates from the observation that the incremental saliency ratio (9) in Fig. 3(c) and in Fig. 6 is a unique identity of each operating point on the dq current plane regardless of the reference frame. Tracking the locus of one such constant isr trajectory in Fig. 6 ensures a stable position observer. Thus, the isr locus can be used as surrogate of the MTPA torque control law.

The block diagram of the proposed LIST position observer is shown in Fig. 7 where the $\hat{d}$-axis current is regulated for isr tracking. This ensures stability as the current references are no longer fixed (for a given torque) in the estimated reference frame but actively adapted to trace the isr locus. Fig. 8 shows the torque distribution as a function of isr to illustrate the overload capability and the deviation from the MTPA trajectory. A low isr has higher torque overload capacity as per Fig. 8 while a high isr provides better signal-to-noise ratio of the position error signal as per (16). As a trade-off, the values $4 \leq isr \leq 7$ are generally recommended. Note that the convergence analysis is only applicable for control schemes with predefined current trajectories as opposed to LIST which actively adapts the reference for isr tracking.
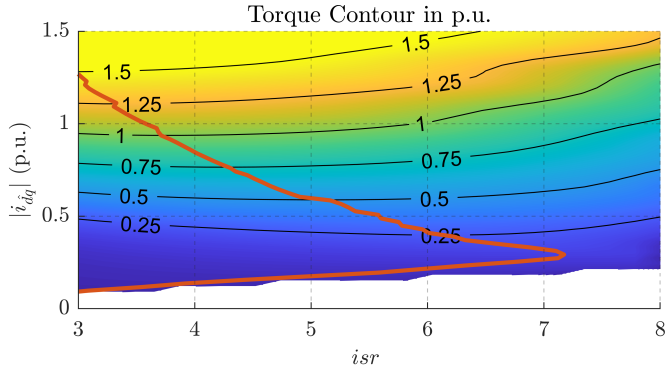
Fig. 8. Torque contour as a function of isr and stator current magnitude to illustrate the torque capability for a selected isr^* reference. Red line is the MTPA trajectory.
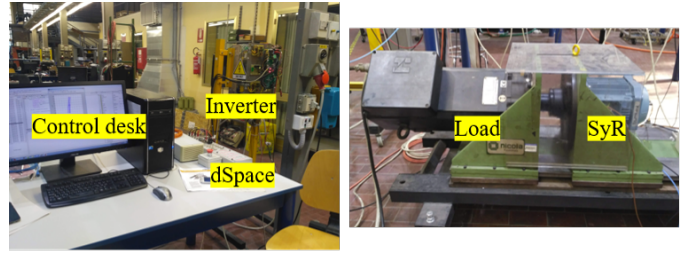

Fig. 9. Experimental Setup of 1.1 kW SyR motor under test on a dSPACE DS1103 control platform at a sampling frequency of 5 kHz.

TABLE I
MOTOR PARAMETERS

Parameters	Symbol	Values	Units
Rated power	P_n	1.1	kW
Rated voltage	V_n	380	V
Rated speed	ω_n	1500	rpm
Rated current	I_n	2.9	A
Rated torque	T_n	7.1	Nm
Pole pairs	p	2	-
Stator resistance	R_s	6.2	Ω
Shaft inertia	J	0.04	kgm^2

B. LIST Implementation

The property of cross-saturation position error is recalled where the maximum and minimum incremental inductance are aligned with the $\hat{d}$ and $\hat{q}$-axes, respectively. A rotating voltage injection is proposed for the inductance estimation in real-time. To reduce the current ripples, an elliptical voltage injection is chosen where the ratio of major to minor axis is equal to the isr^* reference, i.e.,

$$V_h \begin{bmatrix} \cos(\omega_h t) \\ \sin(\omega_h t)/isr^* \end{bmatrix} \qquad (21)$$

where V_h is the magnitude of major-axis of the elliptical voltage injection. This implies that the induced high-frequency current is of the same amplitude on either axis, just big enough to surpass the reliability threshold. The inductances are estimated from the high-frequency current response as

$$\hat{l}'_d = \frac{V_h}{\text{LPF}\{i_{\hat{d}} \cdot 2\sin(\omega_h t)\}} \qquad \hat{l}'_q = \frac{V_h/isr^*}{\text{LPF}\{-i_{\hat{q}} \cdot 2\cos(\omega_h t)\}}. \qquad (22)$$

Note that if the high-frequency ω_h is close to the bandwidth of the current controllers, a phase-shift is incurred in the injected voltage. In such cases, it is recommended to evaluate the net high-frequency amplitude in voltage and current by demodulating both sine and cosine components in either axes as is done in experimental results in the succeeding section.

Following the inductance estimation, the isr control is achieved by regulating the $\hat{d}$-axis current with an integral controller (gain k_r), shown in Fig. 7, as

$$i_d^* = \frac{k_r}{s}\left(isr^* - i\hat{s}r\right) \qquad i\hat{s}r = \frac{\hat{l}'_d}{\hat{l}'_q}. \qquad (23)$$

The $\hat{q}$-axis current reference is determined by the speed controller output scaled by the torque factor k_T (Nm/A) from the nameplate of the machine under test. It is also feasible to adapt the gains of the current controllers using the estimated inductance for a uniform bandwidth at all operating points.

VI. EXPERIMENTAL RESULTS

The proposed LIST position observer is evaluated experimentally with a 1.1 kW SyR motor test-bench on a dSPACE

DS1103 control platform running at a sampling/switching frequency of 5 kHz, as shown in Fig. 9. The parameters of the SyR motor under test are tabulated in Table I.

The DC-link voltage is $v_{dc} = 565$ V. The magnitude of square-wave voltage injection is $V_{sw} = 50$ V. The frequency of the elliptical voltage injection is $\omega = 2\pi \cdot 200$ rad/s; the magnitude of the major axis is $V_h = 100$ V. The LIST reference is $isr^* = 5$ and the integral gain is $k_r = 1$. The PLL gains are tuned for $\Omega_\omega = 2\pi \cdot 25$ rad/s and the estimated speed is low-pass-filtered at 15 Hz. The SyR motor under test is speed-controlled with the load machine torque controlled. Unless otherwise mentioned, the speed controller is tuned for critical damping with the two poles at $\Omega_\omega = 2\pi \cdot 0.5$ rad/s which corresponds to a bandwidth of 1.24 Hz. A minimum current $i_{\hat{d}}^{min} = 0.15$ p.u. is imposed for the saturation of the rotor ribs at no load. Note that in the following results, the real values of the inductances $l'_d \& l'_q$ (and the ratio isr) and the electromagnetic torque T are computed using the reference flux-map LUTs and the rotor position from encoder for comparison with sensorless estimated values.

A. Current Reference Feasibility: Constant $\hat{\gamma}^*$ and $i_{\hat{d}}^*$

The convergence analysis on the feasibility of current reference locus using constant current angle $\hat{\gamma}^* = 70°$ and constant $\hat{d}$-axis current $i_{\hat{d}}^* = 0.25$ p.u. in Figs. 14 and 16 are experimentally corroborated in Figs. 10(a) and 10(b), respectively, with an incremental steps in load torque, $T_L = 0 \to 1.5$ p.u., at an operating speed reference $\omega_r^* = 100$ rpm.

The control becomes unstable shortly after rated torque in Fig. 10(a) due to the lack of zero-up crossing convergence points in Fig. 14. The constant $i_{\hat{d}}$ locus in Fig. 10(b) is stable at overload as predicted in the analysis in Fig. 16. Moreover, the steady-state position error is $\tilde{\theta} \approx 7°$ which is coherent with the analytical estimation in Fig. 16.
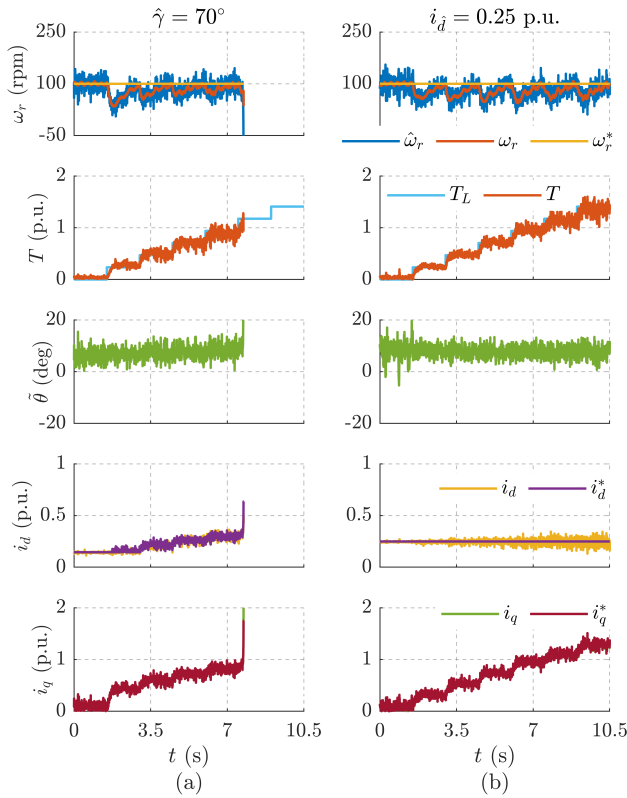
Fig. 10. Feasibility analysis of current reference trajectories with incremental steps in load torque from $T_L = 0 \rightarrow 1.5$ p.u. at speed $\omega_r^* = 100$ rpm: (a) Constant current angle $\hat{\gamma} = 70°$; (b) Constant $\hat{d}$-axis current $i_{\hat{d}} = 0.25$ p.u.

B. LIST Validation

The proposed LIST technique is validated with the incremental steps in load torque at speed reference $\omega_r^* = 100$ rpm, shown in Fig. 11(a). The LIST scheme is observed to be stable at overload operation. Moreover, the estimation of inductance and the isr tracking are effective, showing good correlation with the reference curves.

The ripples in current $i_{\hat{d}}$ and torque T are observed to increase with load; this is due to the diminishing incremental inductance l_d' which increases high-frequency current amplitude. As an alternative to elliptical voltage injection, a rotating high-frequency current injection can be explored using resonant controllers, albeit at the cost of increased complexity.

A load step response with $T_L = 0 \rightarrow 1.5$ p.u. at time $t = 0$ s and standstill condition $\omega_r^* = 0$ is shown in Fig. 11(b). The control is stable and a speed sag of 250 rpm is discerned.

C. Test for Dynamic Stiffness

A rated load torque step response at standstill condition is evaluated for different bandwidths of speed controller; the poles are tuned for $\Omega_\omega = 2\pi \cdot 0.5$ rad/s (bandwidth = 1.24 Hz) and $\Omega_\omega = 2\pi \cdot 1.5$ rad/s (bandwidth = 3.72 Hz) in Figs. 12(a) and 12(b), respectively.

The speed sag for the rated load torque step in Fig. 12(a) is approximately 230 rpm while it is reduced to 150 rpm in Fig. 12(b) at the cost of increased ripples due to the
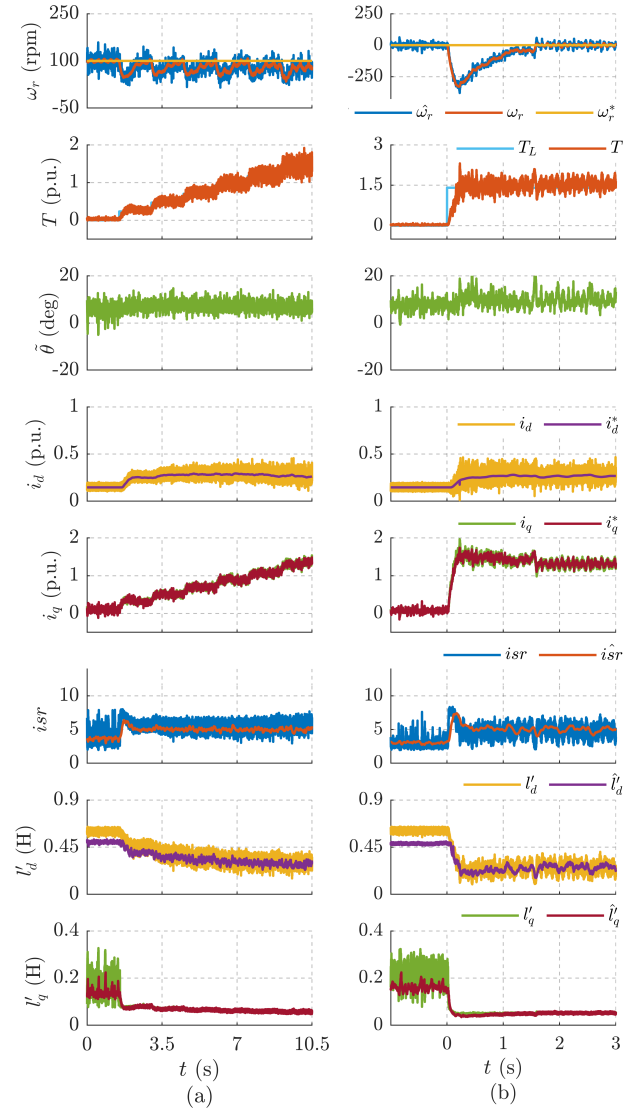

Fig. 11. Proposed LIST validation for $isr^* = 5$: (a) Incremental steps in load torque from $T_L = 0 \rightarrow 1.5$ p.u. at speed $\omega_r^* = 100$ rpm; (b) Load step torque $T_L = 0 \rightarrow 1.5$ p.u. at time $t = 0$ s and standstill condition $\omega_r^* = 0$.

higher bandwidth. Nevertheless, the control stability is not compromised at higher bandwidth. Note that the bandwidth of speed controller is recommended to be equal to or below that of the isr controller to avoid traversing low saliency regions during transients.

D. Speed Dynamic Performance

The speed dynamics is evaluated with a step in reference speed $\omega_r^* = 0 \rightarrow 0.2$ p.u. (300 rpm) at time $t = 0$ s and half-rated load torque $T_L = 0.5$ p.u. in Fig. 13(a). The control is stable and no disruptive transients in position error is observed. For speeds beyond 300 rpm (0.2 p.u.), typically, the back-emf based position estimation is employed.

An overview of the steady-state quantities at speed $\omega_r^* = 100$ rpm and load $T_L = 1.5$ p.u. is shown in Fig. 13(b). The
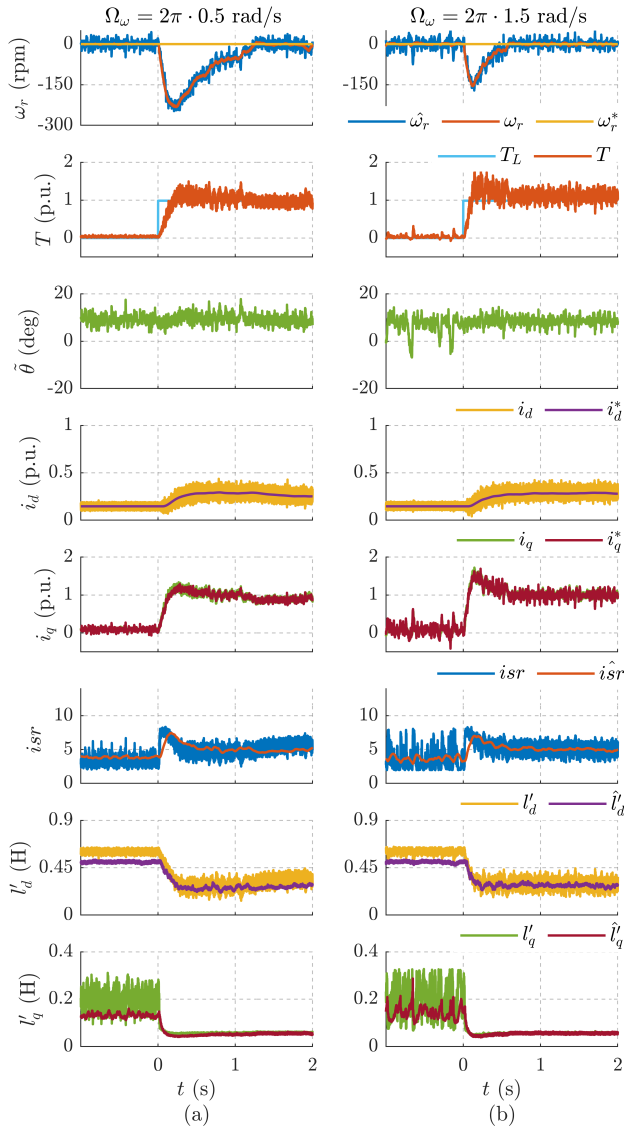
Fig. 12. Test for dynamic stiffness at standstill condition with a rated step in load torque $T_L = 0 \rightarrow 1$ p.u. at time $t = 0$ s for different tuning of speed controller: (a) $\Omega_\omega = 2\pi \cdot 0.5$ rad/s; (b) $\Omega_\omega = 2\pi \cdot 1.5$ rad/s.

stator abc currents are observed to be reasonably sinusoidal in nature despite the overload operation.

VII. CONCLUSION

This paper proposed a new sensorless control technique for the low speeds region without the knowledge of flux-map LUTs of the machine under test. The position estimation uses the conventional pulsating injection along $\hat{d}$-axis with $\hat{q}$-axis current response sent to the PLL, with inevitable cross-saturation position error. The proposed LIST scheme is designed such that the current trajectory traverses along the locus of a constant incremental saliency ratio. To this end, an elliptical voltage injection is used for inductance estimation in real-time and the $\hat{d}$-axis current is regulated to track the isr; the $\hat{q}$-axis current is determined by the speed regulator. This control scheme overcomes the instability related to the cross-saturation effect. Convergence analysis shows that alternatives
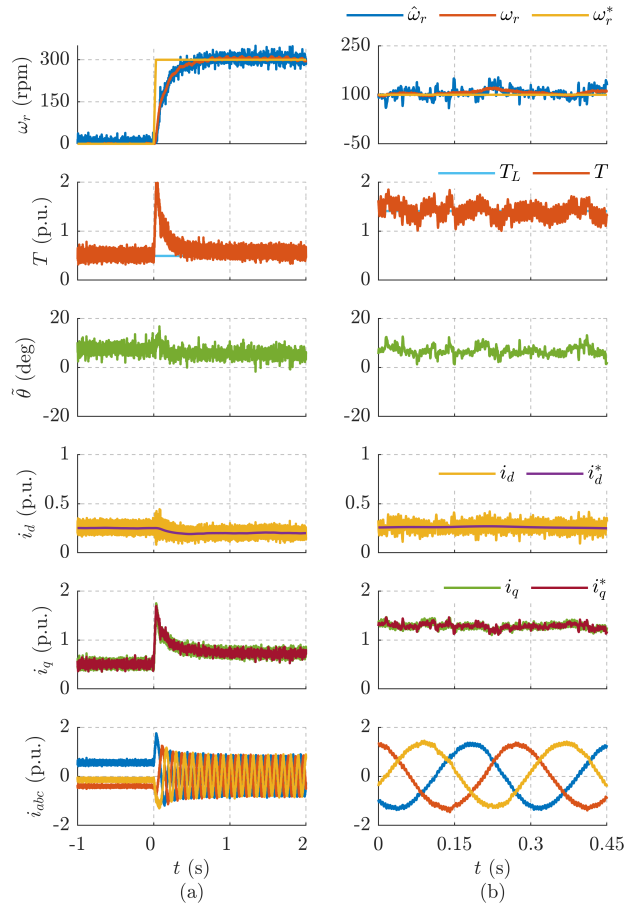

Fig. 13. (a) Speed dynamic performance validation with step speed reference $\omega_r^* = 300$ rpm (0.2 p.u.) at time $t = 0$ s and load $T_L = 0.5$ p.u.; (b) Overview of steady-state quantities at load $T_L = 1.5$ p.u. and speed $\omega_r^* = 100$ rpm.

to the LIST control trajectory such as constant current angle or constant i_d^* reference component are not always feasible. The developed technique is experimentally validated on a 1.1 kW SyR motor test-bench and has demonstrated good overload and dynamic performance to various load torque and speed reference commands.

APPENDIX

A. Feasibility of Constant Current Angle Locus

The convergence analysis for the reference current angle $\hat{\gamma}^* = 70°$ is shown in the position error signal contour plot in Fig. 14. While the rated torque is achievable, the overload condition of 1.5 p.u. torque (dashed white line) remains unrealizable.

B. Feasibility of Constant $\hat{d}$-axis Current Locus

Figs. 15 and 16 show the convergence analysis for the constant locus of $i_{\hat{d}}^* = 0.5$ p.u. and $i_{\hat{d}}^* = 0.25$ p.u., respectively. It is observed in Fig. 15 that the control has poor torque capability and becomes unstable for $|i_{dq}| > 0.6$ p.u. due to the lack of stable zero-up crossing points. On contrary, the locus of lower reference current $i_{\hat{d}}^* = 0.25$ p.u. in Fig. 16 shows
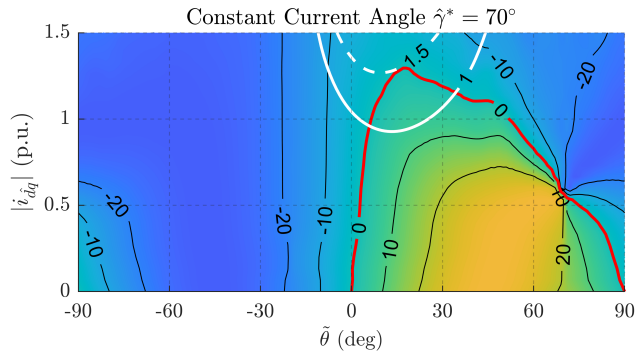
Fig. 14. Position error signal (17) contour for the current references using a constant current angle $\hat{\gamma}^* = 70°$ in the estimated $\hat{d}q$ reference frame. Red line is the zero contour of the error signal. White lines represent the torque contour levels 1 p.u. and 1.5 p.u. (dashed).
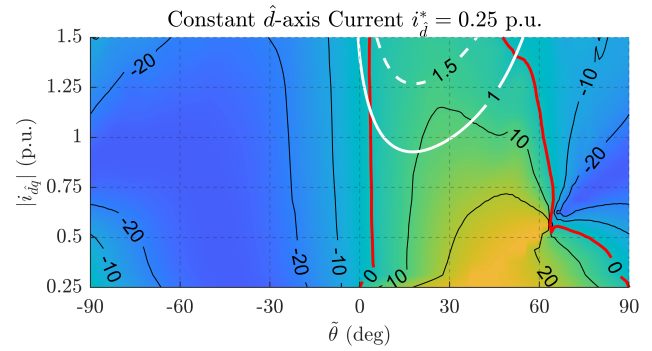
Fig. 16. Position error signal (17) contour for the current references using a constant $\hat{d}$-axis current $i_{\hat{d}}^* = 0.25$ p.u. in the estimated $\hat{d}q$ reference frame. Red line is the zero contour of the error signal. White lines represent the torque contour levels 1 p.u. and 1.5 p.u. (dashed).

Fig. 15. Position error signal (17) contour for the current references using a constant $\hat{d}$-axis current $i_{\hat{d}}^* = 0.5$ p.u. in the estimated $\hat{d}q$ reference frame. Red line is the zero contour of the error signal. White lines represent the torque contour levels 1 p.u. and 1.5 p.u. (dashed).
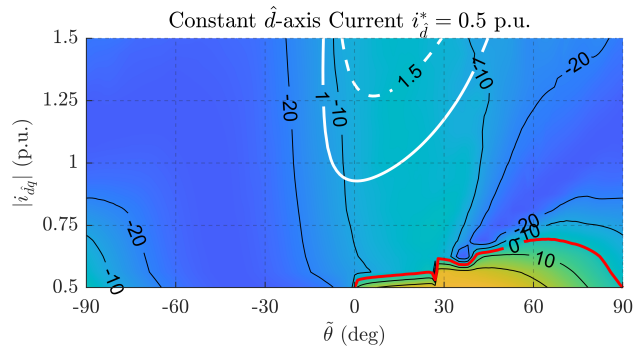
better torque capability including the overload operation. This corroborates the results in Fig. 6 where the locus $i_{\hat{d}}^* = 0.25$ p.u. lies in the green feasible region.

REFERENCES

[1] Y. D. Yoon, S. K. Sul, S. Morimoto, and K. Ide, "High-bandwidth sensorless algorithm for AC machines based on square-wave-type voltage injection," *IEEE Transactions on Industry Applications*, vol. 47, DOI 10.1109/TIA.2011.2126552, no. 3, pp. 1361–1370, 2011.

[2] C. E. Hwang, Y. Lee, and S. K. Sul, "Analysis on position estimation error in position-sensorless operation of IPMSM using pulsating square wave signal injection," *IEEE Transactions on Industry Applications*, vol. 55, DOI 10.1109/TIA.2018.2864117, no. 1, pp. 458–470, 2019.

[3] A. Varatharajan, G. Pellegrino, and E. Armando, "Sensorless Synchronous Reluctance Motor Drives: Auxiliary Flux based Position Observer," *IEEE Journal of Emerging and Selected Topics in Power Electronics*, DOI 10.1109/JESTPE.2020.3019568, p. 1, 2020.

[4] M. Schroedl and P. Weinmeier, "Sensorless control of reluctance machines at arbitrary operating conditions including standstill," *IEEE Transactions on Power Electronics*, vol. 9, DOI 10.1109/63.286816, no. 2, pp. 225–231, 1994.

[5] R. Morales-Caporal and M. Pacas, "Suppression of saturation effects in a sensorless predictive controlled synchronous reluctance machine based on voltage space phasor injections," *IEEE Transactions on Industrial Electronics*, vol. 58, DOI 10.1109/TIE.2010.2080652, no. 7, pp. 2809–2817, Jul. 2011.

[6] A. Varatharajan, P. Pescetto, and G. Pellegrino, "Sensorless Synchronous Reluctance Motor Drives: A Full-Speed Scheme using Finite-Control-Set MPC in a Projection Vector Framework," *IEEE Transactions on Industry Applications*, vol. 56, DOI 10.1109/tia.2020.2990834, no. 4, pp. 3809–3818, 2020.

[7] M. Hinkkanen, P. Pescetto, E. Mölsä, S. E. Saarakkala, G. Pellegrino, and R. Bojoi, "Sensorless Self-Commissioning of Synchronous Reluctance Motors at Standstill Without Rotor Locking," *IEEE Transactions on Industry Applications*, vol. 53, DOI 10.1109/TIA.2016.2644624, no. 3, pp. 2120–2129, 2017.

[8] P. Pescetto and G. Pellegrino, "Automatic Tuning for Sensorless Commissioning of Synchronous Reluctance Machines Augmented with High-Frequency Voltage Injection," *IEEE Transactions on Industry Applications*, vol. 54, DOI 10.1109/TIA.2018.2839600, no. 5, pp. 4485–4493, 2018.

[9] A. Varatharajan, P. Pescetto, and G. Pellegrino, "Sensorless Self-Commissioning of Synchronous Reluctance Machine with Rotor Self-Locking Mechanism," in *2019 IEEE Energy Conversion Congress and Exposition (ECCE)*, DOI 10.1109/ECCE.2019.8913023, pp. 812–817, 2019.

[10] P. Guglielmi, M. Pastorelli, and A. Vagati, "Impact of cross-saturation in sensorless control of transverse-laminated synchronous reluctance motors," *IEEE Transactions on Industrial Electronics*, vol. 53, DOI 10.1109/TIE.2006.870716, no. 2, pp. 429–439, 2006.

[11] D. Mingardi, M. Morandin, S. Bolognani, and N. Bianchi, "On the Proprieties of the Differential Cross-Saturation Inductance in Synchronous Machines," *IEEE Transactions on Industry Applications*, vol. 53, DOI 10.1109/TIA.2016.2622220, no. 2, pp. 991–1000, 2017.

[12] E. Capecchi, P. Guglielmi, M. Pastorelli, and A. Vagati, "Position-sensorless control of the transverse-laminated synchronous reluctance motor," *IEEE Transactions on Industry Applications*, vol. 37, DOI 10.1109/28.968190, no. 6, pp. 1768–1776, 2001.

[13] Y. Li, Z. Q. Zhu, D. Howe, C. M. Bingham, and D. A. Stone, "Improved Rotor-Position Estimation by Signal Injection in Brushless AC Motors, Accounting for Cross-Coupling Magnetic Saturation," *IEEE Transactions on Industry Applications*, vol. 45, DOI 10.1109/TIA.2009.2027518, no. 5, pp. 1843–1850, 2009.

[14] T. Tuovinen and M. Hinkkanen, "Adaptive Full-Order Observer With High-Frequency Signal Injection for Synchronous Reluctance Motor Drives," *IEEE Journal of Emerging and Selected Topics in Power Electronics*, vol. 2, DOI 10.1109/JESTPE.2013.2294359, no. 2, pp. 181–189, 2014.

[15] Z. Q. Zhu, Y. Li, D. Howe, and C. M. Bingham, "Compensation for Rotor Position Estimation Error due to Cross-Coupling Magnetic Saturation in Signal Injection Based Sensorless Control of PM Brushless AC Motors," in *2007 IEEE International Electric Machines & Drives Conference*, vol. 1, DOI 10.1109/IEMDC.2007.383578, pp. 208–213, 2007.

[16] Y. Lee, Y. Kwon, S. K. Sul, N. A. Baloch, and S. Morimoto, "Compensation of position estimation error for precise position-sensorless control of IPMSM based on high-frequency pulsating voltage injection," in *2017 IEEE Energy Conversion Congress and Exposition (ECCE)*, DOI 10.1109/ECCE.2017.8095875, pp. 859–864, 2017.

[17] S. Kuehl, P. Landsmann, and R. M. Kennel, "Compensating angle estimation errors caused by magnetic saturation in anisotropy-based sensorless control schemes," in *3rd IEEE International Symposium on Sensorless Control for Electrical Drives (SLED 2012)*, DOI 10.1109/SLED.2012.6422803, pp. 1–6, 2012.

[18] Y. Kwon, J. Lee, and S. Sul, "Extending Operational Limit of IPMSM

in Signal-Injection Sensorless Control by Manipulation of Convergence Point," *IEEE Transactions on Industry Applications*, vol. 55, DOI 10.1109/TIA.2018.2882483, no. 2, pp. 1574–1586, 2019.

[19] V. Manzolini and S. Bolognani, "On the Rotor Position Self-Sensing Capability of Reluctance and IPM Synchronous Motors," *IEEE Transactions on Industry Applications*, vol. 56, DOI 10.1109/TIA.2020.2984406, no. 4, pp. 3755–3766, 2020.

[20] J. Lee, Y. Kwon, and S. Sul, "Signal-Injection Sensorless Control With Tilted Current Reference for Heavily Saturated IPMSMs," *IEEE Transactions on Power Electronics*, vol. 35, DOI 10.1109/TPEL.2020.2984029, no. 11, pp. 12 100–12 109, 2020.

[21] E. Armando, R. I. Bojoi, P. Guglielmi, G. Pellegrino, and M. Pastorelli, "Experimental identification of the magnetic model of synchronous machines," *IEEE Transactions on Industry Applications*, vol. 49, DOI 10.1109/TIA.2013.2258876, no. 5, pp. 2116–2125, 2013.

Anantaram Varatharajan (M'18) received his B.E.(Honours) degree in electrical and electronics engineering from BITS Pilani University, India, in 2013 and M.Sc. degree in sustainable transportation and electrical power systems (STEPS), an Erasmus Mundus master program from University of Oviedo, Spain, in 2016. He received his Ph.D. (Cum Laude) degree in electrical engineering from Politecnico di Torino, Italy, in 2021.

Dr. Varatharajan is currently a postdoctoral researcher at the department of energy, Politecnico di Torino, Italy. He has over 10 IEEE papers, two patents and one Best Paper Award. His research interests include sensorless and advanced control of synchronous motor drives.

Gianmario Pellegrino (M'06-SM'13) received the MSc and PhD degrees in electrical engineering from Politecnico di Torino, Turin, Italy in 1998 and 2002, respectively. He is currently a Professor of Electrical Machines and Drives at the same university.

He is engaged in several research projects with the industry, and one of the authors of the open-source project SyR-e for the design of electrical motors. He was a visiting fellow at Aalborg University, Denmark, the University of Nottingham, UK, and the University of Wisconsin-Madison, USA. Dr. Pellegrino is an Associate Editor for the IEEE Transactions on Industry Applications and an IEEE Senior Member. He has 50 IEEE journal papers, two patents and seven Best Paper Awards.

Dr. Pellegrino is a member of the Power Electronics Interdepartmental Laboratory (PEIC) established in 2017 at the Politecnico di Torino and a member of the Advisory Board of PCIM (Power Conversion and Intelligent Motion) Europe. He is currently the Vice President of the CMAEL (Convertitori, Macchine e Azionamenti Elettrici) Association, representative of the scholars in Power Converters, Electrical Machines and Drives in Italy, and the Rector's Advisor for Interdepartmental Centres of Politecnico di Torino.

Guilherme Bueno Mariani received double engineering degree in electrical engineering in 2012 from the Grenoble-INP and from UNESP. In 2016 he received a Ph.D degree in electrical engineering from the University of Grenoble Alpes. Since 2016, he is a researcher engineering at the Power Electronics Systems division at Mitsubishi Electric Research Centre Europe, Rennes, France. His present research interest is with the control, modeling and simulation of electrical machines

Nicolas Voyer was born in Saint-Brieuc, France, in 1972. He graduated from Telecom ParisTech in 1995 in digital communications.

From 1997 to 2008, he was a research engineer in Mitsubishi Electric Information Technology Europe, Rennes, France and was involved in the design and standardization of 3G and 4G cellular systems. Since 2008, he has been in the Power Electronic System Division of Mitsubishi Electric Research Centre Europe, Rennes, France. He is the author of more than 80 patents. His present interests include the simulation and modelling of power electronic systems, including PV, HVDC, EV and railway traction systems.

Akira Satake was born in 1961, and joined Mitsubishi Electric in 1985, after receiving the B.E. degree from Tokyo University, Japan.

His research has been focused on motor drive technologies, including controls for mechatronics components and power-electronic circuits. In 2014, he received R&D100 awards with the development of Sensor-less Servo Drive Unit & Motor, which is a new product of his company for factory automation. He is currently a chief engineer for motor drive technology in Advanced Technology R&D Center of Mitsubishi Electric Corporation.